THE JOURNAL OF PHYSICAL CHEMISTRY C

Article

Cite This: J. Phys. Chem. C 2018, 122, 18356−18364

pubs.acs.org/JPCC

On the Use of Photocurrent Imaging To Determine Carrier Diffusion Lengths in Nanostructured Thin-Film Field-Effect Transistors

Rui Xiao,[†] Yasen Hou,[†] Matt Law,[‡,§] and Dong Yu*[,†]

[†]Department of Physics, University of California Davis, 1 Shields Avenue, Davis, California 95616, United States

[‡]Department of Chemical Engineering and Materials Science and [§]Department of Chemistry, University of California Irvine, Irvine, California 92697, United States

Supporting Information

ABSTRACT: Scanning photocurrent microscopy (SPCM) has been widely used as a powerful experimental technique to investigate charge transport and recombination in nanostructured field-effect transistors (FETs). Photocurrent mapping modulated by transverse electric field provides critical insights into local electronic band bending and carrier transport. However, the analysis of experimental results is often based on unjustified assumptions. In particular, the inhomogeneous carrier concentration induced by gate bias and local photoexcitation may significantly influence the photocurrent distribution, but these effects have not been considered in previous work. Furthermore, carrier lifetime is a function of carrier concentration and can have a large spatial variation in a gated channel, which may lead to further complication. Here, we perform rigorous two-dimensional cross-sectional modeling of thin-film FETs under local photoexcitation. Our simulation results validate that accurate minority carrier diffusion lengths can be extracted from SPCM measurements regardless of the substantial nonuniformity in carrier density and potential that is characteristic of these devices. However, at high excitation intensity, the photocurrent decay lengths deviate from the minority carrier diffusion lengths as a result of light-induced carrier drift. We also verify that thermoelectric effects due to laser heating can be ignored. By accounting for a carrier concentration-dependent recombination lifetime, we find that the photocurrent decay length corresponds to an average diffusion length of carriers distributed throughout the channel. Although we focus here on colloidal quantum dot thin films, our conclusions can be extended to SPCM measurements of any thin-film or nanowire FET.

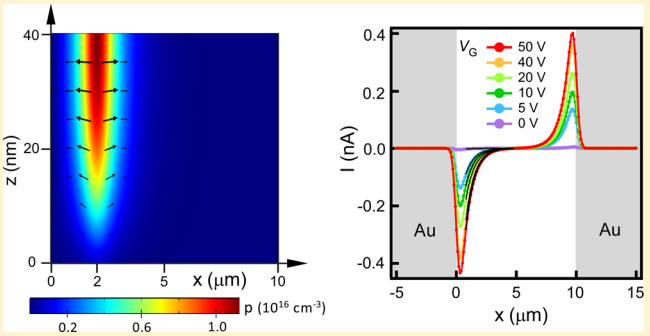

1. INTRODUCTION

The past few decades have witnessed the rapid development of nanostructured materials, which not only offer fascinating platforms for fundamental understanding of physics and chemistry in confined systems of reduced dimensions but have also opened up new opportunities for novel optoelectronic applications such as solar cells, photodetectors, light-emitting devices, and lasers. For example, nanowires (NWs) and quantum dots (QDs) exhibit unique optoelectronic properties that can be tuned to optimize solar energy conversion. In addition, solar cells based on efficient multiple exciton generation in QDs[1,2] may overcome the Shockley−Queisser limit (33%). However, the low carrier mobility (μ) in QD thin films (10^{-3} to 10 cm^2/V s) is a bottleneck for electronic applications of these materials.[3−5] For solar energy applications, one of the most critical factors related to mobility is the minority carrier diffusion length ($L_D = \sqrt{\mu\tau k_B T/q}$, where τ is the carrier recombination lifetime, k_B is the Boltzmann constant, T is the temperature, and q is the fundamental charge). An L_D much longer than the transport length is essential for highly efficient charge collection. A reliable experimental extraction of this parameter in nanostructured materials is highly desirable for understanding charge transport and enhancing device performance.

Scanning photocurrent microscopy (SPCM) is a powerful experimental technique that can be used to obtain valuable information on band alignment, charge transport, and dynamics in semiconductors. In a SPCM setup, a tightly focused laser beam is raster-scanned across the surface of a planar electronic device while the photocurrent is recorded as a function of illumination position. The photocurrent mapping obtained from SPCM can be used to extract physical parameters such as electric field distribution and minority carrier diffusion lengths. SPCM is often combined with a field-effect transistor (FET) configuration, where a gate voltage is applied to modulate the carrier concentration. SPCM and electron beam-induced current, which is based on a similar principle, have recently been applied to explore nanotubes,[6,7] NWs,[8−20] two-dimensional (2D) materials,[21,22] and QD thin films.[23,24]

Received: July 13, 2018
Published: July 18, 2018

DOI: 10.1021/acs.jpcc.8b06734
J. Phys. Chem. C 2018, 122, 18356−18364

Despite the widespread application of SPCM, data interpretation is often not rigorously justified, which may yield ambiguous conclusions. The photocurrent can be created by several different mechanisms, including majority/minority carrier drift and diffusion and photoinduced thermoelectric effects. Previous simulation efforts[10] based on one-dimensional (1D) modeling have shown that minority carrier diffusion is dominant if the device has at least one Schottky junction because the majority carriers are blocked by the Schottky junction and the minority carrier drift term is small at zero bias. However, the 1D modeling is not suitable for describing a gated channel, which has a transverse carrier concentration gradient. The situation is further complicated by nonuniform carrier generation because of attenuation and interference of the laser beam. Inhomogeneity due to gating and localized illumination may create transverse carrier flow. Such effects were not taken into account in the previous 1D model and may significantly influence the photocurrent distribution, resulting in inaccurate extraction of minority carrier diffusion lengths. 2D simulation has been previously performed,[25] but the work was mainly on understanding band bending at the hetero-structured junctions, instead of extraction of carrier diffusion lengths. Furthermore, the laser intensity used in SPCM is often much higher than solar intensity. This high irradiance creates a large number of excess charge carriers that can alter the local electric field distribution and cause local heating that drives thermoelectric currents. Finally, the carrier recombination lifetime often sensitively depends on the carrier concentration,[15,24] resulting in a spatially varying lifetime in a gated nanostructure device. All of these effects must be considered to fully understand the SPCM results under realistic experimental conditions.

2. COMPUTATIONAL DETAILS

In this article, we have developed a rigorous and comprehensive 2D cross-sectional model for nanostructured thin-film FETs under local photoexcitation. We focus on QD thin-film FETs, but our conclusions are relevant to other nanostructured systems. QD thin films are treated as a bulk semiconductor with a quantum confinement-enhanced band gap and the simulation is based on a continuum model. A finite element mesh size of 1−2 nm is used in the simulation. Realistic physical parameters such as band gap, carrier effective mass, doping concentration, carrier mobility, and lifetime are used and the simulation results are compared with recent experimental results.[24] COMSOL Multiphysics, a commonly used finite element solver equipped with the heat-transfer module and the semiconductor module, is used to solve the 2D steady-state thermal transport (eq 1), electrostatic (eq 2), and charge continuity equations (eqs 3 and 4)

$$\nabla^2 T + Q/\kappa = 0 \tag{1}$$

$$\varepsilon \nabla^2 V = -q(p - n + N_D - N_A) \tag{2}$$

$$\frac{1}{q}\nabla \cdot J_n + G - R = 0 \tag{3}$$

$$J_n = -q\mu_n n \nabla V + \mu_n k_B T \nabla n - q\mu_n n S_n \nabla T \tag{4}$$

where Q is the heat power density, n (p) is the electron (hole) concentration, J_n is the electron current density, the charge recombination rate (R) is assumed to be dominated by the Shockley−Read−Hall (SRH) mechanism, and the spatially varying charge carrier generation rate (G) corresponds to the local laser excitation with a Gaussian profile. The hole current density J_p has a similar form as J_n but carries positive charge. Simulation parameters are listed in Table 1. Boundary

Table 1. Simulation Parameters

symbol	physical meaning	value	reference
E_g	bandgap	0.7 eV	24
N_D	donor concentration	10^{16} to 10^{18} cm^{-3}	[a]
N_A	acceptor concentration	0	[a]
N_C	density of states at conduction band edge	4.4×10^{18} cm^{-3}	26
N_V	density of states at valence band edge	4.4×10^{18} cm^{-3}	26
l	channel length	10 μm	[a]
w	channel width	100 μm	[a]
κ	thermal conductivity of QD thin film	2.5 W/(m K)	24
S_n	electron Seebeck coefficient of QD thin film	−1.0 mV/K or variable	24
ϵ_r	dielectric constant of QD thin film	12	27
m_e [a]	electron effective mass	$0.15m_0$	28
m_h [a]	hole effective mass	$0.15m_0$	28
τ_p	hole lifetime	10−1000 ns or variable	[a]29
τ_n	electron lifetime	10−1000 ns or variable	[a]29
μ_p	hole mobility	0.2−20 cm^2/(V s)	[a]30
μ_n	electron mobility	0.2−20 cm^2/(V s)	[a]30
$q\Phi_B$	Schottky barrier height	0.1−0.55 eV	[a]
λ	laser wavelength	532 nm	[a]
σ	laser beam width	10, 250 nm	[a]
I_{ex}	laser peak intensity	0.08−80 W/cm^2	[a]
α	absorption coefficient of QD thin film at 532 nm	1.35×10^5 cm^{-1}	31

[a]Experimental values with the range representing different samples and measurements.

conditions include (1) vertical current density vanishes at the surfaces of the QD thin film in contact with air and SiO_2 and (2) the barrier height ($q\Phi_B = E_C - q\Phi_m$, where E_C is the conduction band edge and $q\Phi_m$ is the contact metal work function) at the interface between the QD thin film and the Au electrode is set to 0.1 eV. Although a barrier height that is too large results in nonlinear $I-V_{SD}$ curves inconsistent with the experimental observation (Figure S1a,b in the Supporting Information), a barrier height that is too small essentially yields Ohmic contact which does not allow extraction of carrier diffusion lengths by SPCM.[10] Our device configuration mimics the PbSe QD thin-film FETs[24] with a 40 nm thick PbSe QD thin film on a 300 nm thick SiO_2 layer on a Si substrate (Figure 1a). The 40 nm thick source and drain Au electrodes are separated by 10 μm. A gradual change of the film thickness near the edges of the electrodes (Figure 1d) is used to mimic the actual film morphology observed in scanning electron microscopy images.

3. RESULTS AND DISCUSSION

3.1. Dark Characteristics. We first present the simulated current−voltage ($I-V$) characteristics of a QD thin-film FET in the dark. The current versus source-drain bias ($I-V_{SD}$) curves at different gate voltages (V_G) (Figure 1b) indicate that the device is an n-channel FET, consistent with the acceptor

DOI: 10.1021/acs.jpcc.8b06734
J. Phys. Chem. C 2018, 122, 18356−18364

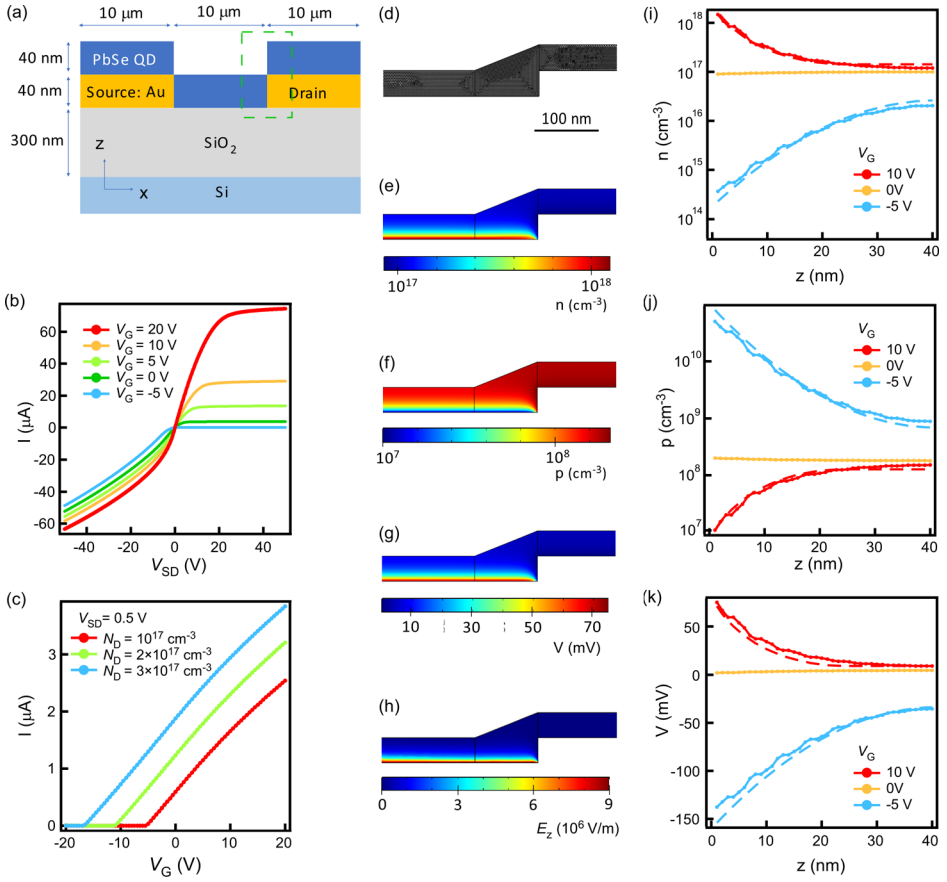

Figure 1. Simulated carrier density, electric potential, and electric field distributions and current−voltage curves for a PbSe QD thin-film FET without photoexcitation. (a) Schematic of the PbSe QD thin-film FET (not to scale). The region outlined in the green dashed box is shown in (d). (b) Simulated $I-V_{SD}$ curves at various V_G, with $N_D = 1 \times 10^{17}$ cm^{-3} and a channel width of 100 μm. (c) Simulated $I-V_G$ curves at $V_{SD} = 0.5$ V and $N_D = 1$ to 3×10^{17} cm^{-3}. (d−h) Maps (to scale) showing (from top to bottom) the finite element mesh configuration, electron density, hole density, potential, and vertical electric field E_z, respectively, in the QD thin film at $V_G = 10$ V and $V_{SD} = 0$ V. (i−k) Electron, hole, and potential distributions along the z-axis at $x = 5$ μm (in the middle of the channel) and $V_{SD} = 0$ V. The dashed curves are calculated from analytical expressions.

and donor concentrations set in the simulation. From the $I-V_G$ curves (Figure 1c), an electron field-effect mobility of $\mu_n^* = 1.7$ cm^2/V s is estimated by

$$\mu_n^* = \frac{dI}{dV_G}\frac{l^2}{V_{SD}C_{OX}} \quad (5)$$

where l is the distance between source and drain electrodes and C_{OX} is the capacitance of SiO_2 as estimated from an ideal parallel plate capacitor configuration. μ_n^* is close to the electron mobility value used in the simulation ($\mu_n = 2$ cm^2/V s). The slight discrepancy may be caused by an overestimation of C_{OX} used in eq 5 because in reality, the thin film is not a metal and hence not all of the gate-induced carriers are at the bottom surface of the film as is assumed for a parallel plate capacitor.[32] The fringe electric fields near the contacts may lead to further deviation from the ideal parallel plate model. The $I-V_G$ curves are simulated at various N_D values (Figure 1c). Although the slope remains the same, the threshold voltage shifts to more negative values as N_D increases because a more negative V_G is needed to deplete the additional electrons. In the SPCM simulations below, we fix N_D at 1×10^{17} cm^{-3} to be consistent with experimental results (Figure S1c in the Supporting Information).

The simulation allows us to visualize the gate-induced inhomogeneity in both charge carrier and potential distributions (Figure 1d−k). At $V_G = 10$ V, the electron concentration near the dielectric interface increases to 2×10^{18} cm^{-3} but remains close to the bulk value of 1×10^{17} cm^{-3} at the top surface of the film (Figure 1i). The accumulation layer has a thickness about 10 nm, which is about two QD layers. This is consistent with a simple estimation from the Debye length $\sqrt{\frac{\epsilon_0\epsilon_r k_B T}{q^2 N_D}} = 13$ nm (using $\epsilon_r = 12$ for the QD film)[27] and a previous estimation in the literature.[5] In comparison, the depletion region at $V_G = -5$ V is more extended than the accumulation layer, where electron concentration is altered throughout the entire film thickness, ranging from 4×10^{14} cm^{-3} near the dielectric surface to 2×10^{16} cm^{-3} near the top surface (Figure 1i). This is expected because of the weaker charge screening in depletion. The hole concentration at $V_G = -5$ V increases substantially to 5×10^{10} cm^{-3} (Figure 1j) but does not reach the ambipolar regime where both electrons and holes contribute to conduction, in agreement with the $I-V_G$ curves. This substantial inhomogeneity in carrier concentration is associated with a potential gradient. The potential varies over 70 mV across the thin film at $V_G = 10$ V and over 100 mV at $V_G = -5$ V (Figure 1k). The simulated n, p, and V distributions are all consistent with those calculated from

DOI: 10.1021/acs.jpcc.8b06734
J. Phys. Chem. C 2018, 122, 18356−18364

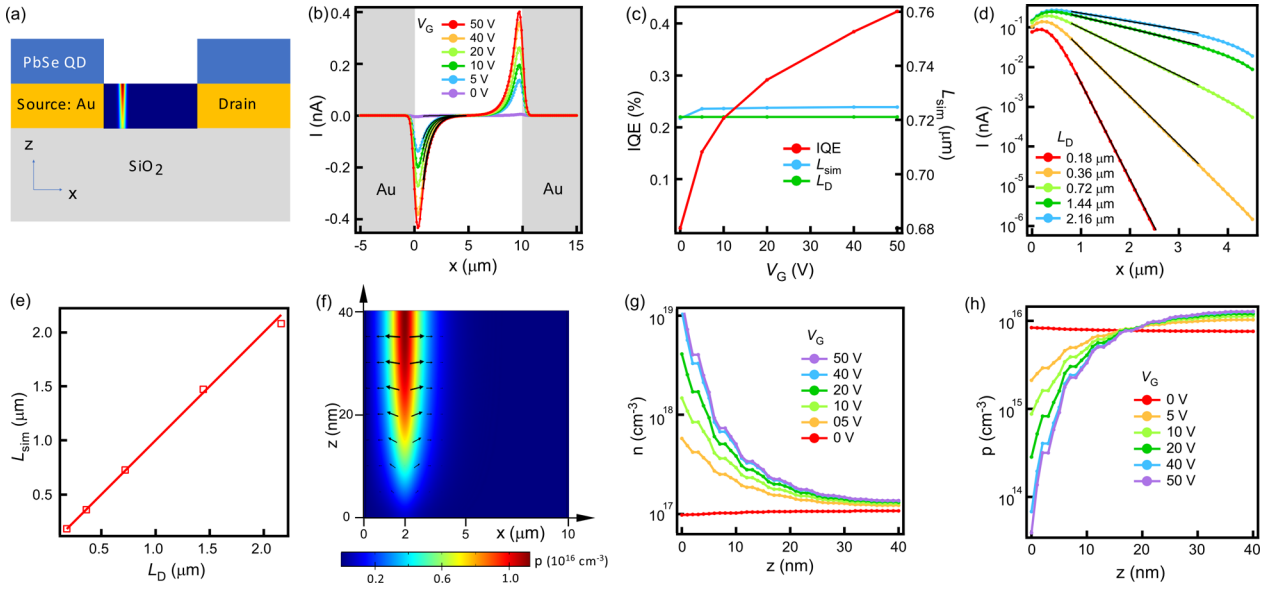

Figure 2. Simulated photocurrent distribution in a PbSe QD FET with local photoexcitation. All simulations are performed at V_{SD} = 0 V. (a) Schematic of a typical device illuminated by a focused laser beam. The color map between the source and drain represents the distribution of carrier generation as the laser if centered at x = 2 μm. (b) Photocurrent as a function of photoexcitation position at various V_G, with I_{ex} = 0.8 W/cm^2 and L_D = 0.72 μm. The shaded areas indicate the Au contacts. The black curves are exponential fittings. (c) IQE at the maximum photocurrent position and L_{sim} extracted from (b) as a function of V_G. (d) Semilog plots of photocurrent vs photoexcitation position with different L_D. The black curves are exponential fittings. (e) L_{sim} exacted from (d) vs L_D. The squares are simulated values and the line is the fitting. (f) Hole concentration map in the channel at V_G = 10 V. The arrows represent the hole current density vector J_p. (g,h) Vertical distribution of electron and hole concentration at the laser injection point (x = 2 μm) for different V_G.

analytical expressions (dashed curves in Figure 1i–k) as detailed in the Supporting Information. The potential gradient results in a strong vertical electric field E_z on the order of 10^4 V/cm at the bottom of the film. Such a field can create a substantial transverse drift current. In addition, the amount of band bending at the contacts depends on z (Figure S1d), which may lead to different charge separation efficiencies. All of these effects should be considered in SPCM analysis.

3.2. Photocurrent Distributions. Next, we simulate photocurrent as a function of photoexcitation position at V_{SD} = 0 V and various V_G. The absorption coefficient of the QD thin film at 532 nm is $\alpha = 1.35 \times 10^5$ cm^{-1}.[31] Carrier multiplication and optical interference are not considered here. The charge carrier generation rate is $G(x, z) = G_0 \exp\left(-\frac{(x-x_0)^2}{2\sigma^2} - \alpha z\right)$ as shown in Figure 2a, where $G_0 = I_{ex}\alpha/h\nu$ is the peak generation rate, I_{ex} is the peak laser intensity, $h\nu$ is the photon energy, x_0 is the center of the laser spot, and σ = 250 nm is the Gaussian beam width. We find that the photocurrent increases with increasing V_G as a result of greater band bending at the contacts and higher channel conductivity (Figure 2b). Photocurrent drops to zero when photoexcitation is on top of the contacts, where the gate field is screened and band bending is small. As a result, photogenerated carriers recombine without contributing to the photocurrent. The internal quantum efficiency (IQE), defined as the ratio of electrons collected to photons absorbed in the QD film, is calculated at the maximum current position and increases with V_G (Figure 2c). The low IQE values are caused by the small barrier heights, which will be discussed in detail later. The simulated photocurrent distribution follows an exponential decay except for the round-off near the electrodes and near the middle of the channel (Figure 2b,d). The former is caused by the finite laser spot size and the latter by the finite channel length (the symmetry requires the photocurrent to be zero at the mid-channel). Exponential fits using $I = I_0 \exp\left(-\frac{x}{L_{sim}}\right)$ yield a gate-independent photocurrent decay length (L_{sim}) that is in excellent agreement with the minority carrier diffusion length (L_D) value calculated from the simulation parameters μ_p and τ_p ($L_D = \sqrt{\mu_p \tau_p k_B T/q}$, Figure 2c).

The above simulation results clearly demonstrate that SPCM can be used to extract accurate minority carrier diffusion lengths in thin-film FETs, even when the gate bias creates strong inhomogeneity in both electron and hole concentrations through the channel (Figure 2f–h). This is perhaps surprising, as the carrier inhomogeneity can lead to current (including both diffusion and drift) perpendicular to the channel and complicate the simple 1D transport picture. Although boundary conditions require current density to be horizontal at the top and the bottom surfaces, in the channel, the vertical component is not necessarily zero. Indeed, a significant vertical component of the minority carrier (hole) current is found in our simulation (Figure 2f). On the other hand, the region for the strong vertical current component is only limited close to the injection position. The current density vector J_p (including both drift and diffusion components), shown as the black arrows in Figure 2f, quickly becomes horizontal at positions away from the injection position (x = 2 μm). J_{pz}/J_{px} decays to ~10^{-2} at 0.6 μm and ~10^{-4} at 1.8 μm away from injection (Figure S3a). As confirmed by our simulation, the carriers flow parallel to the channel in most of the transport path except near the injection point. Therefore, the 2D carrier transport can be simplified into 1D and the diffusion length can still be accurately extracted, even with gate and excitation-induced inhomogeneity.

DOI: 10.1021/acs.jpcc.8b06734
J. Phys. Chem. C 2018, 122, 18356–18364

To generalize the conclusion that the photocurrent decay length measured in SPCM is equal to minority carrier diffusion length, we have performed simulations for a broad range of parameters, including film thickness, doping concentration, carrier lifetime, and mobility. In all cases, L_{sim} is in excellent agreement with L_D. We find close equivalence between L_{sim} and L_D for a wide range of L_D and film thickness (Figure S2 in the Supporting Information). The photocurrent distributions simulated at fixed μ_p (2 cm^2/V s) but various τ_p (ranging from 6.25 to 900 ns) all show exponential decays with decay lengths in agreement with L_D (Figure 2d,e). L_{sim} and L_D are also consistent for various doping concentrations (Figure S4). Figure 3a,c shows that when the majority carrier (electron) mobility varies by 2 orders of magnitude (μ_n = 0.2−20 cm^2/V s), the photocurrent decay length remains the same, as long as the minority carrier (hole) mobility is fixed. In contrast, with fixed electron mobility, varying hole mobility (μ_p = 0.2−20 cm^2/V s in Figure 3b,d) results in a significant change in the photocurrent decay length (L_{sim} = 0.23−2.06 μm), which is in agreement with L_D. The slight discrepancy when electron/hole mobilities are substantially mismatched can be understood by the photo-Dember effect,[33] where the unbalanced electron and hole mobilities create different electron and hole distributions and result in an internal electric field. As an example, when μ_p = 10μ_n, L_{sim} is slightly shorter than L_D (Figure 3d). This is because photogenerated holes have a broader distribution than electrons. Consequently, an internal electric field pointing toward the laser injection position is formed, which reduces the photocurrent decay length.

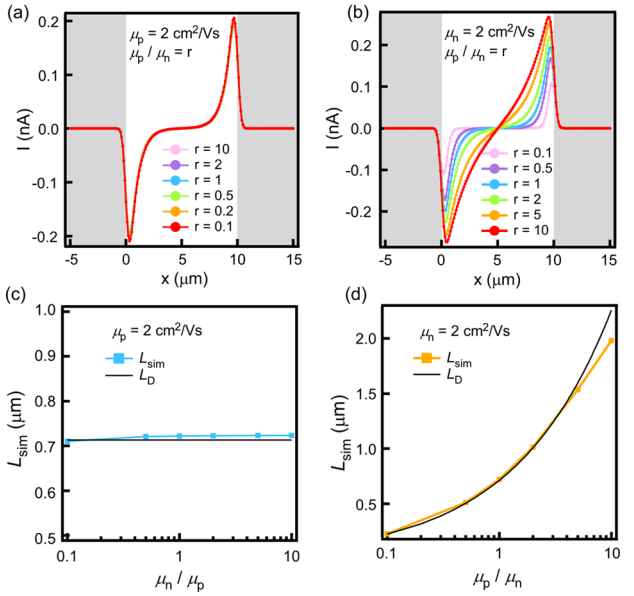

Figure 3. Simulated photocurrent distribution with mismatching electron/hole mobilities. Simulations are performed at V_{SD} = 0 V, V_G = 10 V, and I_{ex} = 0.8 W/cm^2. (a,b) Simulated photocurrent as a function of the electron/hole mobility ratio. The simulations are performed with fixed carrier lifetime (τ_n = τ_p = 100 ns). The ratio r = 0.1−10 corresponds to μ_p/μ_n. (c,d) L_{sim} extracted from (a,b), comparing with the calculated L_D.

3.3. Interference Effects. We now turn our attention to the effects of optical interference. In the previous simulation, photogeneration is assumed to follow the Beer−Lambert law (exponential attenuation of light with distance). In reality, optical waves reflected by the SiO_2 and Si surfaces interfere with the incoming wave, causing a more complicated generation profile, as shown in Figures 4a,b and S5. Carrier generation rate $G(z)$ is obtained from optical modeling following a previous study.[31] In a real device, a 20 nm thick Al_2O_3 layer is coated on the QD thin film and is considered when calculating $G(z)$. We then fit $G(z)$ with polynomial functions up to the fifth term, input the fitting functions as the carrier generation profile in COMSOL, and simulate new photocurrent distributions. We find that the photocurrent is insensitive to the details of the vertical generation profile that results from interference. Exponential optical decays and interference patterns with different SiO_2 thicknesses yield essentially the same photocurrent distribution (Figure 4c). The photocurrent decay lengths L_{sim} match L_D in all three cases. This result is expected because vertical inhomogeneity created by the gate or the optical field causes insignificant vertical carrier flow. The hole current density indeed remains largely parallel to the channel even with interference (Figure 4a,b insets), with J_{pz}/J_{px} < 0.01 (Figure S3b,c). The fact that the photocurrent distribution is insensitive to the vertical generation profile ensures that SPCM can be used to extract the carrier diffusion length.

We have also excluded the possibility that the photocurrent distribution is caused by photon scattering or lateral wave-guiding within the FET structure. For example, photons may travel from the injection point toward the contacts via a guided wave in the SiO_2 layer. However, finite difference time domain

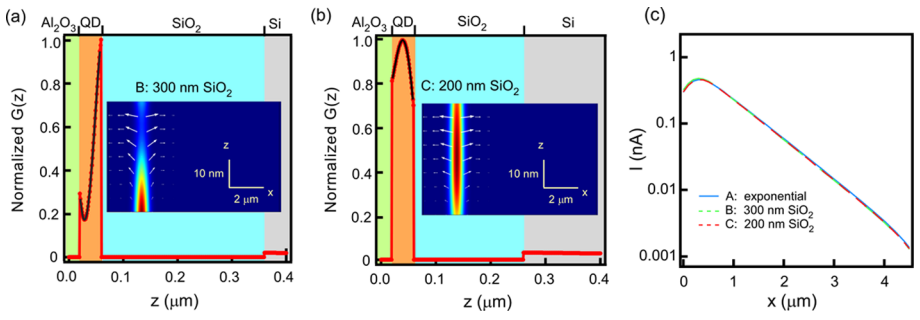

Figure 4. Thin-film optical interference effects. (a,b) Distribution of normalized generation rate with 300 and 200 nm SiO_2, respectively, at photoexcitation wavelength λ = 532 nm. The black curves are polynomial fittings. Insets [not in scale, rotated 90° from the background (a,b)]: 2D profiles of generation in the channel. The arrows represent J_p. All simulations are performed at V_{SD} = 0 V. (c) Simulated photocurrent as a function of photoexcitation position with optical interference included. Three types of carrier generation distributions are considered: (A) exponential decay, (B) interference pattern with 300 nm SiO_2, and (C) interference pattern with 200 nm SiO_2. The three curves match perfectly.

DOI: 10.1021/acs.jpcc.8b06734
J. Phys. Chem. C 2018, 122, 18356−18364

(FDTD) simulations show that the light absorbed in the depletion region near the contacts is too little to account for the observed photocurrent distribution (Figure S6). As the photoexcitation is moved away from the junction, absorption in the depletion region drops with a decay length of 0.13 μm, much shorter than the experimentally observed photocurrent decay length (up to 1.7 μm).[24]

3.4. Intensity Dependence. Because SPCM is often carried out at high laser intensity, understanding how photocurrent distribution depends on intensity is important for achieving accurate estimates of L_{sim} with this method. We simulated photocurrent distributions at various peak photoexcitation intensities from 0.08 to 80 W/cm^2 (Figure 5a). At

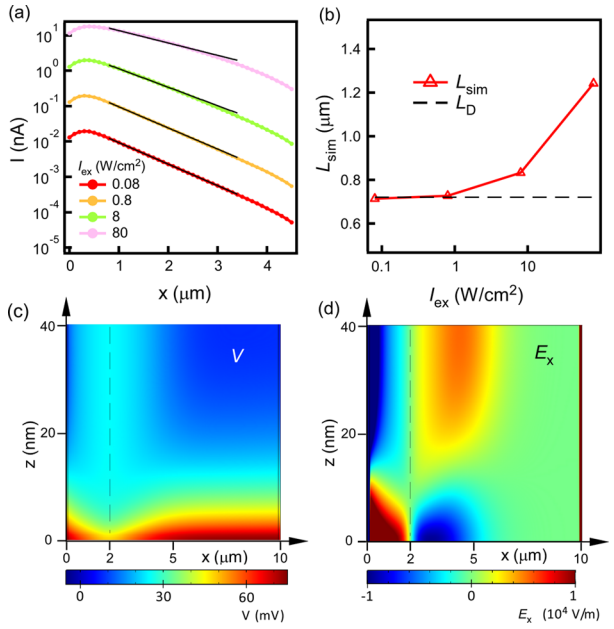

Figure 5. Simulated photocurrent distributions with high-intensity photoexcitation at V_{SD} = 0 V. (a) Photocurrent as a function of photoexcitation position with different laser intensities, V_G = 10 V, and L_D = 0.72 μm. (b) Fitted decay length L_{sim} in comparison to L_D for different laser intensities. (c,d) Simulated distributions of V and E_x at I_{ex} = 80 W/cm^2 injected at x = 2 μm (shown as dashed vertical lines).

relatively low laser intensity (0.08−0.8 W/cm^2), L_{sim} is in good agreement with L_D, whereas at higher laser intensity (8−80 W/cm^2), longer photocurrent decay is clearly observed. L_{sim} increases from 0.72 μm at 0.08 W/cm^2 to 1.39 μm at 80 W/cm^2 (Figure 5b). The longer L_{sim} at high intensity is attributed to the photoexcitation-induced electric field that drives carriers to travel farther. Figure 5d shows the horizontal electric field (E_x) map at I_{ex} = 80 W/cm^2. We find that E_x is as large as 10^2 V/cm and has opposite polarity on the two sides of the excitation position. The holes are repelled to the top of the film by the positive gate bias and their lateral diffusion leads to electric field pointing away from the photogeneration point, whereas the electrons are attracted to the bottom, leading to the electric field pointing toward the photogeneration point. The holes at the top are then driven by the light-induced electric field to drift further toward the left contact. When the electric field is sufficiently high at high intensity, L_D becomes smaller than the minority carrier drift length $L_E = \mu_p \tau_p E$.[11] The threshold electric field at which $L_E = L_D$ is given by $E_{th} = k_B T/(qL_D) = 3.6 \times 10^2$ V/cm, comparable to the simulated E_x at 80 W/cm^2 (Figure 5d). Longer photocurrent decay at high light intensity has been experimentally observed in NW FETs.[11] High intensity may even cause band bending flipping and a reversal of the photocurrent polarity in extreme cases.[17]

At low intensity, E_x is small compared to E_{th} and carrier transport is still dominated by diffusion (E_x maps at different intensities are shown in Figure S7). Therefore, SPCM can be used to accurately determine L_D, under the condition that the photogenerated carrier concentration is much lower than the dark majority carrier concentration, that is, $\Delta n \ll n$. Otherwise, photogeneration would lead to a substantial change in local band bending and a strong internal electric field, which results in carrier drift and a longer decay length ($L_{sim} > L_D$). The photogenerated electron concentration can be estimated by $\Delta n = \frac{\alpha I_{ex} \tau_n}{h\nu}$, where τ_n = 100 ns is the electron lifetime used in the simulation for Figure 5. To have Δn comparable to $n = 1 \times 10^{17}$ cm^{-3}, I_{ex} must be larger than 2.7 W/cm^2. This is consistent with the simulation results showing that L_{sim} starts to deviate from L_D as I_{ex} is above similar intensity (Figure 5b).

3.5. Photoheating Effects. In addition to the diffusion current and electric field-induced drift current, local photoexcitation causes thermoelectric current (temperature gradient-induced drift, last term in eq 4) that may dominate the total current in certain situations.[34] In the above simulations, we ignored this term and will now justify that the thermoelectric current is indeed small. We first solve the thermal transport equation (eq 1) to obtain the temperature distribution. The heating power density is set to be $Q = h\nu G$, where G is the

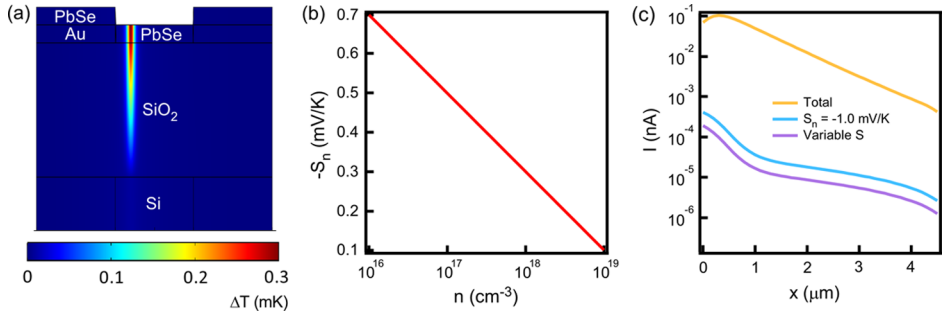

Figure 6. Photoheating-induced thermoelectric effects. (a) Simulated temperature distribution with I_{ex} = 0.8 W/cm^2 at x = 2 μm. Dimensions are as shown in Figure 1a. (b) Seebeck coefficient as a function of n calculated from eq 6. (c) Simulated distributions of the total photocurrent and the thermoelectric component at V_{SD} = 0 V, V_G = 10 V, and I_{ex} = 0.8 W/cm^2. Two types of Seebeck coefficients are considered: S_n = −1.0 mV/K and n-dependent S_n as in (b).

DOI: 10.1021/acs.jpcc.8b06734
J. Phys. Chem. C 2018, 122, 18356−18364

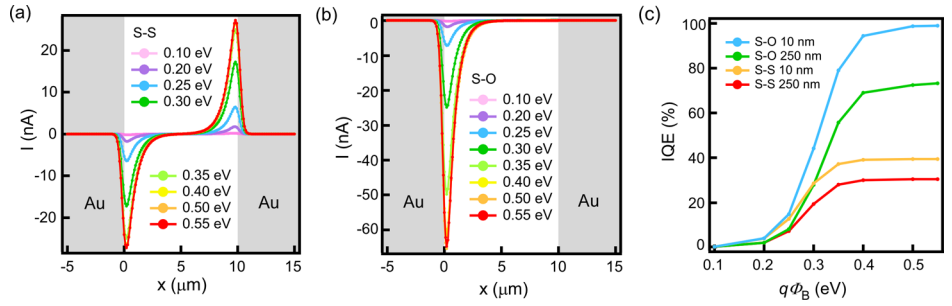

Figure 7. Quantum efficiency as a function of Schottky barrier height $q\Phi_B$ at V_{SD} = 0 V. (a,b) Simulated photocurrent profiles at different $q\Phi_B$ with I_{ex} = 0.8 W/cm^2 and V_G = 10 V for Schottky−Schottky (S−S) and Schottky−Ohmic (S−O) devices, respectively. (c) IQE as function of $q\Phi_B$ for S−S and S−O devices with different beam widths σ.

carrier generation rate considering interference with 300 nm SiO_2. This is an overestimation as not all photon energy contributes to heating. We then constrain the bottom and side surfaces of the FET substrate to be at room temperature as boundary conditions. Thermal transport across the film/air interface is assumed to be convective. According to the simulations, local excitation with I_{ex} = 0.8 W/cm^2 at x = 2 μm results in a maximum temperature increase of only 0.3 mK (Figure 6a). This result is consistent with a simple estimation considering only vertical thermal transfer through SiO_2 to Si, which is assumed to be at room temperature because Si is a good thermal conductor. We may then estimate the temperature increase in the QD thin film as $\Delta T = \frac{I_{ex}\Delta d}{\kappa_{OX}}$ = 0.4 mK, where η = 0.22 is the fraction of the light absorbed in the film, d = 300 nm is the thickness of SiO_2, and κ_{OX} = 1.3 W/(m K) is the thermal conductivity of SiO_2. The estimated temperature is slightly higher than the simulated value, presumably because lateral thermal transport in the QD thin film and thermal losses to the air are not considered in this simple estimate.

Next, we solve the charge transport equations (eqs 2−4) including the thermoelectric term using the simulated temperature distribution. Carrier concentration-dependent Seebeck coefficients are used, giving

$$S_n = -\frac{k}{q}\frac{\left[2.5 - s + \ln\left(\frac{N_C}{n}\right)\right]n\mu_n}{n\mu_n + p\mu_p} \quad (6)$$

$$S_p = \frac{k}{q}\frac{\left[2.5 - s - \ln\left(\frac{N_V}{p}\right)\right]p\mu_p}{n\mu_n + p\mu_p} \quad (7)$$

where the parameter s = 1/2 is appropriate for phonon scattering (s = 3/2 for impurity scattering).[26] The calculated S_n values as shown in Figure 6b are consistent with the experimentally measured values in PbSe QD thin films.[35,36] The simulated thermoelectric current is 3 orders of magnitude smaller than the photovoltaic current (Figure 6c). The simulation result is consistent with simple estimation by calculating the thermoelectric current using $I = S_n\Delta T/R \approx$ 0.3 pA, where S_n = 0.7 mV/K, ΔT = 0.3 mK, and the thin-film resistance $R = (1/nq\mu_n)\cdot(l/A)$ = 0.8 MΩ are used. This is indeed 3 orders of magnitude smaller than the photovoltaic current of 0.1 nA. Therefore, the thermoelectric current can be ignored in SPCM measurements of PbSe QD films, as long as the temperature is not too high to significantly change the physical parameters such as Seebeck coefficient, carrier mobility, and lifetime.

3.6. Barrier Height Dependence. Although our simulations convincingly demonstrate that SPCM can be used to extract the carrier diffusion length, the simulated IQE values are quite low (<1% in Figure 2c). The low IQE is not favorable for experimental measurements or photovoltaic applications. We now aim to understand the low IQE and propose a practical method to increase its value. The low IQE is caused by the small barrier height ($q\Phi_B$ = 0.1 eV) and the large series resistance of the channel ($R \approx$ 0.8 MΩ) that we used in the above simulations. To study the IQE, we performed additional simulations of two types of FETs: (1) S−S devices with two Schottky contacts and (2) a S−O device with one Schottky and one Ohmic contact. The simulated IQE values reach up to 31% for the S−S device and 74% for the S−O device (Figure 7c) when using a Gaussian beam with σ = 250 nm. The IQE values approach their ideal limits (40% for S−S and 99% for S−O) if a narrower beam with σ = 10 nm is used (Figures 7c and S8a,b). The 40% IQE (instead of 50%) for the S−S device is caused by the series channel resistance and an equivalent circuit diagram calculation quantitatively agrees with the simulated IQE values (Figure S8c,d). The larger beam size gives a smaller IQE because photoexcitation partially occurs in the thin film on top of the metal contacts. Experimentally, the larger barrier heights can be achieved by replacing Au contacts with lower work function metals such as Ti or Al.

3.7. Spatially Varying Lifetime. In the above simulations, carrier lifetime was kept constant throughout the thin film. In reality, lifetime is a function of carrier concentration. We consider a simple model in which carrier recombination is dominated by the SRH mechanism assisted by trap states at a single energy level. This is reasonable as the recombination in these films is dominated by a nonradiative process. The recombination rate is[37]

$$R_{SRH} = \frac{pn - n_i^2}{\tau_{p_0}\left(n + n_i\exp\left(\frac{E_R - E_i}{k_BT}\right)\right) + \tau_{n_0}\left(p + n_i\exp\left(-\frac{E_R - E_i}{k_BT}\right)\right)} \quad (8)$$

where n_i is the intrinsic electron concentration, E_i is the mid-gap energy, E_R is the trap energy, $\tau_{p_0} = 1/(\nu_{th}\sigma_p N_R)$, $\nu_{th} = \sqrt{3k_BT/m_h^*}$, σ_p is the hole capture cross section, and N_R is the density of the trap sites (τ_{n_0} has a similar definition

DOI: 10.1021/acs.jpcc.8b06734
J. Phys. Chem. C 2018, 122, 18356−18364

with p replaced by n). In the approximation of low injection, the electron and hole lifetimes are[37]

$$\tau_p = \frac{\tau_{n_0}(p_0 + p') + \tau_{p_0}[n_0 + n' + N_R(1 + n_0/n')^{-1}]}{n_0 + p_0 + N_R(1 + n_0/n')^{-1}(1 + n'/n_0)^{-1}} \quad (9)$$

$$\tau_n = \frac{\tau_{p_0}(n_0 + n') + \tau_{n_0}[p_0 + p' + N_R(1 + p_0/p')^{-1}]}{n_0 + p_0 + N_R(1 + p_0/p')^{-1}(1 + p'/p_0)^{-1}} \quad (10)$$

where $n_0 = N_C \exp[(E_F - E_C)/k_BT]$ and $p_0 = N_V \exp[(E_V - E_F)/k_BT]$ are the free-electron and hole densities, respectively, and $n' = N_C \exp[(E_R - E_C)/k_BT]$ and $p' = N_V \exp[(E_V - E_R)/k_BT]$ are the densities of free electrons and holes, respectively, when $E_F = E_R$. Figure 8a shows τ_p in the n-type film and τ_n in the p-type film as a function of E_F, taking $N_R = 1 \times 10^{18}$ cm^{-3}, which corresponds to 0.2 trap sites per QD, $E_C - E_R = 0.1$ eV, and $\sigma_p = \sigma_n = 1.1 \times 10^{-18}$ cm^2. As E_F shifts down from E_C to E_i, τ_p increases by several orders of magnitude. The inhomogeneous carrier distribution induced by the gate field and local excitation then gives rise to a spatially varying lifetime (Figure 8b). A lower value of N_D (=10^{15} cm^{-3}) is used in Figure 8 to have a large variation of lifetime. Under positive V_G, τ_p is much shorter at the bottom of the film because of the higher electron concentration. The simulated photocurrent distributions at various V_G can still be fit to exponential decays (Figure 8c) suitable for extracting L_{sim}. L_{sim} decreases significantly at higher V_G (Figure 8d) because the hole lifetime is reduced as n increases, in agreement with experimental results.[24] The L_{sim} values lie between the expected L_D using τ_p values near the top and bottom surfaces of the film. These results suggest that SPCM actually measures the average minority carrier diffusion length in nanostructured FETs as a result of a spatially varying carrier lifetime.

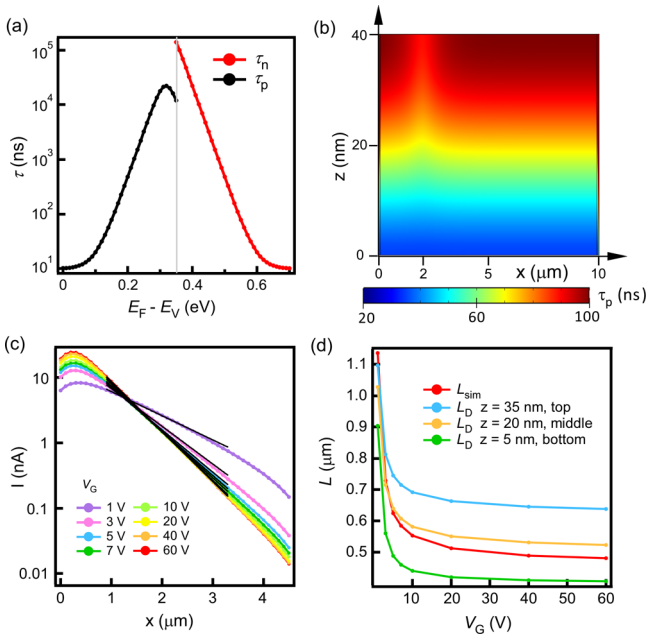

Figure 8. Photocurrent distributions simulated with n-dependent lifetime at $V_{SD} = 0$ V. (a) Electron and hole lifetimes as functions of E_F. The gray vertical line indicates the mid-gap. (b) τ_p distribution in the thin-film channel with $I_{ex} = 0.8$ W/cm^2 at $x = 2$ μm and $V_G = 10$ V. (c) Photocurrent as a function of photoexcitation position at various V_G. The black curves are exponential fittings. (d) V_G-dependent L_{sim} extracted from (c) and L_D calculated from τ_p at different z.

4. CONCLUSIONS

In conclusion, we have performed rigorous 2D modeling for QD thin-film FETs with local photoexcitation. Our simulation results clearly show that SPCM can be used to extract minority carrier diffusion lengths even when gate bias and local photoexcitation induce substantial inhomogeneity in the charge carrier and electric potential distributions, as long as the laser intensity is sufficiently low. High-intensity photoexcitation may create local band bending that leads to longer photocurrent decay. A substantial electron/hole mobility mismatch may create minor error in diffusion length extraction because of the photo-Dember effect. Photothermoelectric effects can be ignored because of efficient heat dissipation through SiO_2 to Si in the FET structure. Quantum efficiency can be greatly enhanced by increasing the junction barrier height, approaching to unity in a device with only one Schottky contact. If carrier lifetime sensitively depends on the carrier concentration, then the photocurrent decay lengths correspond to an average of the minority carrier diffusion lengths throughout the thin film. This work provides confirmation and guidance for interpreting SPCM results and employing photocurrent imaging to determine important charge transport characteristics of gated thin-film and NW devices.

■ ASSOCIATED CONTENT

Supporting Information

The Supporting Information is available free of charge on the ACS Publications website at DOI: 10.1021/acs.jpcc.8b06734.

PbSe nanocrystal synthesis and thin-film preparation; additional COMSOL simulation results on $I-V_{SD}$ curves at different barrier heights; analytical expressions for calculating potential and carrier distributions; photocurrent distributions with various minority carrier diffusion length values, film thicknesses, and barrier heights; optical modeling considering interference in QD thin films; FDTD simulation results to evaluate the photon propagation mechanism; and equivalent circuit model for calculating IQE (PDF)

■ AUTHOR INFORMATION

Corresponding Author

*E-mail: yu@physics.ucdavis.edu.

ORCID

Dong Yu: 0000-0002-8386-065X

Notes

The authors declare no competing financial interest.

■ ACKNOWLEDGMENTS

This work was supported by the UC Office of the President under the UC Laboratory Fees Research Program Collaborative Research and Training Award LFR-17-477148. D.Y. and R.X. acknowledge the U.S. National Science Foundation Grant DMR-1710737 and DMR-1838532.

DOI: 10.1021/acs.jpcc.8b06734
J. Phys. Chem. C 2018, 122, 18356−18364

REFERENCES

(1) Schaller, R. D.; Klimov, V. I. High Efficiency Carrier Multiplication in PbSe Nanocrystals: Implications for Solar Energy Conversion. *Phys. Rev. Lett.* **2004**, *92*, 186601.

(2) Semonin, O. E.; Luther, J. M.; Choi, S.; Chen, H.-Y.; Gao, J.; Nozik, A. J.; Beard, M. C. Peak External Photocurrent Quantum Efficiency Exceeding 100% Via MEG in a Quantum Dot Solar Cell. *Science* **2011**, *334*, 1530−1533.

(3) Yu, D.; Wang, C.; Guyot-Sionnest, P. N-Type Conducting CdSe Nanocrystal Solids. *Science* **2003**, *300*, 1277−1280.

(4) Talapin, D. V.; Murray, C. B. PbSe Nanocrystal Solids for N- and P-Channel Thin Film Field-Effect Transistors. *Science* **2005**, *310*, 86−89.

(5) Liu, Y.; Tolentino, J.; Gibbs, M.; Ihly, R.; Perkins, C. L.; Liu, Y.; Crawford, N.; Hemminger, J. C.; Law, M. PbSe Quantum Dot Field-Effect Transistors with Air-Stable Electron Mobilities above 7 cm2 V-1 s-1. *Nano Lett.* **2013**, *13*, 1578−1587.

(6) Freitag, M.; Tsang, J. C.; Bol, A.; Yuan, D.; Liu, J.; Avouris, P. Imaging of the Schottky Barriers and Charge Depletion in Carbon Nanotube Transistors. *Nano Lett.* **2007**, *7*, 2037−2042.

(7) Ahn, Y. H.; Tsen, A. W.; Kim, B.; Park, Y. W.; Park, J. Photocurrent Imaging of p−n Junctions in Ambipolar Carbon Nanotube Transistors. *Nano Lett.* **2007**, *7*, 3320−3323.

(8) Ahn, Y.; Dunning, J.; Park, J. Scanning Photocurrent Imaging and Electronic Band Studies in Silicon Nanowire Field Effect Transistors. *Nano Lett.* **2005**, *5*, 1367−1370.

(9) Kelzenberg, M. D.; Turner-Evans, D. B.; Kayes, B. M.; Filler, M. A.; Putnam, M. C.; Lewis, N. S.; Atwater, H. A. Photovoltaic Measurements in Single-Nanowire Silicon Solar Cells. *Nano Lett.* **2008**, *8*, 710−714.

(10) Fu, D.; Zou, J.; Wang, K.; Zhang, R.; Yu, D.; Wu, J. Electrothermal Dynamics of Semiconductor Nanowires under Local Carrier Modulation. *Nano Lett.* **2011**, *11*, 3809−3815.

(11) Graham, R.; Miller, C.; Oh, E.; Yu, D. Electric Field Dependent Photocurrent Decay Length in Single Lead Sulfide Nanowire Field Effect Transistors. *Nano Lett.* **2011**, *11*, 717−722.

(12) Gutsche, C.; Niepelt, R.; Gnauck, M.; Lysov, A.; Prost, W.; Ronning, C.; Tegude, F.-J. Direct Determination of Minority Carrier Diffusion Lengths at Axial GaAs Nanowire P-N Junctions. *Nano Lett.* **2012**, *12*, 1453−1458.

(13) Mohite, A. D.; Perea, D. E.; Singh, S.; Dayeh, S. A.; Campbell, I. H.; Picraux, S. T.; Htoon, H. Highly Efficient Charge Separation and Collection across in Situ Doped Axial VLS-Grown Si Nanowire P-N Junctions. *Nano Lett.* **2012**, *12*, 1965−1971.

(14) Soudi, A.; Hsu, C.-H.; Gu, Y. Diameter-Dependent Surface Photovoltage and Surface State Density in Single Semiconductor Nanowires. *Nano Lett.* **2012**, *12*, 5111−5116.

(15) Yang, Y.; Li, J.; Wu, H.; Oh, E.; Yu, D. Controlled Ambipolar Doping and Gate Voltage Dependent Carrier Diffusion Length in Lead Sulfide Nanowires. *Nano Lett.* **2012**, *12*, 5890−5896.

(16) Graham, R.; Yu, D. Scanning Photocurrent Microscopy In Semiconductor Nanostructures. *Mod. Phys. Lett. B* **2013**, *27*, 1330018.

(17) Yang, Y.; Peng, X.; Yu, D. High Intensity Induced Photocurrent Polarity Switching in Lead Sulfide Nanowire Field Effect Transistors. *Nanotechnology* **2014**, *25*, 195202.

(18) Triplett, M.; Yang, Y.; Léonard, F.; Talin, A. A.; Islam, M. S.; Yu, D. Long Minority Carrier Diffusion Lengths in Bridged Silicon Nanowires. *Nano Lett.* **2015**, *15*, 523−529.

(19) Xiao, R.; Hou, Y.; Fu, Y.; Peng, X.; Wang, Q.; Gonzalez, E.; Jin, S.; Yu, D. Photocurrent Mapping in Single-Crystal Methylammonium Lead Iodide Perovskite Nanostructures. *Nano Lett.* **2016**, *16*, 7710−7717.

(20) Hou, Y.; Xiao, R.; Tong, X.; Dhuey, S.; Yu, D. In Situ Visualization of Fast Surface Ion Diffusion in Vanadium Dioxide Nanowires. *Nano Lett.* **2017**, *17*, 7702−7709.

(21) Xia, F.; Mueller, T.; Golizadeh-Mojarad, R.; Freitag, M.; Lin, Y.-m.; Tsang, J.; Perebeinos, V.; Avouris, P. Photocurrent Imaging and Efficient Photon Detection in a Graphene Transistor. *Nano Lett.* **2009**, *9*, 1039−1044.

(22) Wu, C.-C.; Jariwala, D.; Sangwan, V. K.; Marks, T. J.; Hersam, M. C.; Lauhon, L. J. Elucidating the Photoresponse of Ultrathin MoS2 Field-Effect Transistors by Scanning Photocurrent Microscopy. *J. Phys. Chem. Lett.* **2013**, *4*, 2508−2513.

(23) Strasfeld, D. B.; Dorn, A.; Wanger, D. D.; Bawendi, M. G. Imaging Schottky Barriers and Ohmic Contacts in PbS Quantum Dot Devices. *Nano Lett.* **2012**, *12*, 569−575.

(24) Otto, T.; Miller, C.; Tolentino, J.; Liu, Y.; Law, M.; Yu, D. Gate-Dependent Carrier Diffusion Length in Lead Selenide Quantum Dot Field-Effect Transistors. *Nano Lett.* **2013**, *13*, 3463−3469.

(25) Howell, S. L.; Jariwala, D.; Wu, C.-C.; Chen, K.-S.; Sangwan, V. K.; Kang, J.; Marks, T. J.; Hersam, M. C.; Lauhon, L. J. Investigation of Band-Offsets at Monolayer-Multilayer MoS2 Junctions by Scanning Photocurrent Microscopy. *Nano Lett.* **2015**, *15*, 2278−2284.

(26) Sze, S. M.; Ng, K. K. *Physics of Semiconductor Devices*, 3d ed.; Wiley-Interscience, 2007.

(27) Luther, J. M.; Law, M.; Beard, M. C.; Song, Q.; Reese, M. O.; Ellingson, R. J.; Nozik, A. J. Schottky Solar Cells Based on Colloidal Nanocrystal Films. *Nano Lett.* **2008**, *8*, 3488−3492.

(28) Aziza, A.; Amzallag, E.; Balkanski, M. Free electron effective mass in PbSe and PbSnSe mixed crystals. *Solid State Commun.* **1970**, *8*, 873−877.

(29) An, J. M.; Franceschetti, A.; Zunger, A. The Excitonic Exchange Splitting and Radiative Lifetime in PbSe Quantum Dots. *Nano Lett.* **2007**, *7*, 2129−2135.

(30) Talgorn, E.; Gao, Y.; Aerts, M.; Kunneman, L. T.; Schins, J. M.; Savenije, T. J.; van Huis, M. A.; van der Zant, H. S. J.; Houtepen, A. J.; Siebbeles, L. D. A. Unity quantum yield of photogenerated charges and band-like transport in quantum-dot solids. *Nat. Nanotechnol.* **2011**, *6*, 733−739.

(31) Law, M.; Beard, M. C.; Choi, S.; Luther, J. M.; Hanna, M. C.; Nozik, A. J. Determining the Internal Quantum Efficiency of PbSe Nanocrystal Solar Cells with the Aid of an Optical Model. *Nano Lett.* **2008**, *8*, 3904−3910.

(32) Khanal, D. R.; Wu, J. Gate Coupling and Charge Distribution in Nanowire Field Effect Transistors. *Nano Lett.* **2007**, *7*, 2778−2783.

(33) Gu, P.; Tani, M.; Kono, S.; Sakai, K.; Zhang, X.-C. Study of Terahertz Radiation from InAs and InSb. *J. Appl. Phys.* **2002**, *91*, 5533−5537.

(34) Xu, X.; Gabor, N. M.; Alden, J. S.; van der Zande, A. M.; McEuen, P. L. Photo-Thermoelectric Effect at a Graphene Interface Junction. *Nano Lett.* **2010**, *10*, 562−566.

(35) Shanker, G. S.; Swarnkar, A.; Chatterjee, A.; Chakraborty, S.; Phukan, M.; Parveen, N.; Biswas, K.; Nag, A. Electronic Grade and Flexible Semiconductor Film Employing Oriented Attachment of Colloidal Ligand-Free PbS and PbSe Nanocrystals at Room Temperature. *Nanoscale* **2015**, *7*, 9204−9214.

(36) Yang, D.; Lu, C.; Yin, H.; Herman, I. P. Thermoelectric Performance of PbSe Quantum Dot Films. *Nanoscale* **2013**, *5*, 7290−7296.

(37) Bube, R. H. *Photoconductivity of Solids*; John Wiley & Sons, Inc.: New York, 1960; p 312−314.

DOI: 10.1021/acs.jpcc.8b06734
J. Phys. Chem. C 2018, 122, 18356−18364